

## Passive Tracer Dispersion by Idealized Flows across Rossby Numbers

MADHAV SIROHI<sup>a</sup> AND JIM THOMAS<sup>a,b</sup>

<sup>a</sup> International Centre for Theoretical Sciences, Tata Institute of Fundamental Research, Bangalore, India  
<sup>b</sup> Centre for Applicable Mathematics, Tata Institute of Fundamental Research, Bangalore, India

(Manuscript received 14 July 2023, in final form 22 April 2024, accepted 23 April 2024)

**ABSTRACT:** In this work, we compare and contrast the phenomenological changes in passive tracer dispersion at asymptotically small to  $O(1)$  Rossby numbers using idealized two-dimensional flows generated by a two-vertical-mode model. With increasing flow Rossby numbers, we find that the forward flux of tracer variance increases monotonically and the tracer variance spectra show severe depletion of the tracer field, indicating enhanced stirring of the tracer by higher Rossby number flows. On examining the physical structure of the tracer flux and its connection to strain- and vorticity-dominant regions in the flow, we find that a major share of the tracer flux is located in high-shear, strain-dominant regions between coherent vortices at low Rossby numbers, while at higher Rossby numbers, the tracer flux is primarily located in vorticity-dominant regions that are composed of fragmented bits of vorticity. The tracer field is anticorrelated with the tracer flux, i.e., tracer variance is higher in physical regions where tracer flux is lower and vice versa. Our results highlight multiple anisotropic features of submesoscales that enhance tracer dispersion at  $O(1)$  Rossby numbers and emphasize the need to take these into account while developing parameterizations for large-scale models.

**KEYWORDS:** Turbulence; Small scale processes; Mixing

### 1. Introduction

Oceanic flows stir tracers such as heat, salt, and carbon from large scales where tracers are forced to small scales where they are mixed and homogenized. The features of tracer stirring strongly depend on the spatial scale considered. This means that lateral stirring at 100-km scales, 10-km scales, and 1-km scales will be generically different. Furthermore, since oceanic general circulation models are often set at coarse resolutions, tracer stirring processes by flows that are underresolved need to be parameterized using prespecified tracer diffusivities, which in turn have profound effects on model outputs. For instance, lateral diffusivity of tracers prescribed in ocean models can affect circulation strength and carbon uptake (Gnanadesikan et al. 2015; Ragen et al. 2020; Busecke and Abernathy 2019; Chouksey et al. 2022). Consequently, an in-depth understanding of tracer stirring at different scales is needed to develop accurate parameterizations for large-scale ocean models.

The  $O(100)$ -km mesoscale oceanic flow is characterized by asymptotically small Rossby numbers and is dominated by geostrophically and hydrostatically balanced coherent eddies. Since the balanced mesoscale contains close to 90% of the flow kinetic energy (Ferrari and Wunsch 2009), significant efforts in the past have been channelized to study fundamental features of tracer dispersion using idealized quasigeostrophic and related models (Holloway and Kristmannsson 1984; Klein et al. 1998; Scott 2006; Smith and Ferrari 2009). Despite the undisputed role mesoscale flows play in large-scale dynamics, the last two decades have seen a revolution in recognizing the importance of submesoscale dynamics in oceanography. In situ measurements and ocean model outputs have revealed

the prominent presence of submesoscale flows in different oceanic regions, these flows being characterized by  $O(1)$  Rossby numbers and an increased departure from balanced dynamics (Capet et al. 2008; Shcherbina et al. 2013; Brannigan et al. 2015; Thompson et al. 2016; Poje et al. 2017; Yu et al. 2019; Siegelman et al. 2020). Submesoscale flows with  $O(1)$  Rossby number are seen in many different scenarios, such as those generated in weakly sheared mixed layers, steep topographic regions, internal gravity wave-dominant regions, and regions with fronts, for example (McWilliams 2016; Gula et al. 2015; Clément et al. 2016; Lien and Sanford 2019; Thomas 2023; Boccaletti et al. 2007). Intriguingly, submesoscale tracer dispersion characteristics are seen to depart from the predictions of geostrophic turbulence theories.

Passive tracer variance spectra have been analyzed from multiple oceanic observational datasets (Vladoiu et al. 2022; Spiro Jaeger et al. 2020; Klymak et al. 2015; Cole and Rudnick 2012; Samelson and Paulson 1988), and these datasets indicate significant variability in spectral slopes, thereby departing from predictions of geostrophic turbulence theories. Flows that stir and disperse tracer fields faster will expel tracer variance from a particular scale to smaller scales at a faster rate, leading to the depletion of tracer variance at that particular scale and eventually to steeper tracer variance spectra. Consequently, steeper tracer spectra reported in these studies are an indication that the stirring processes that operate at submesoscales are much more efficient than those that would result from geostrophic turbulence in the small Rossby number regime. The steeper spectra could be a result of enhanced horizontal stirring due to the presence of internal waves, other ageostrophic modes, or frontogenetic processes, while shallower spectra could be a result of nonlocal stirring (Scott 2006; Smith and Ferrari 2009; Kunze et al. 2015; Vladoiu et al. 2022). On a similar note, oceanic cruises that perform dye dispersion experiments time and again report significant

Corresponding author: Jim Thomas, jimthomas.edu@gmail.com

variability in the diffusivity estimates, with the observed diffusivity oftentimes being an order of magnitude or more than what is expected from theory (Shcherbina et al. 2015; Sundermeyer et al. 2020; Kunze et al. 2015; Polzin and Ferrari 2004). Notably, some of these studies emphasize findings of  $O(1)$  Rossby numbers in their observational sites, hinting at the contribution of ageostrophic flow components on tracer dispersion.

The above suggests that the tracer dispersion characteristics are different for submesoscale and mesoscale flows. Although a broad set of studies have examined mesoscale tracer dispersion in idealized settings, much less is understood regarding the role of submesoscale flows on tracer dispersion. Part of the difficulty lies in the fact that submesoscale flows are generated in a wide variety of settings, making it challenging to identify common generic characteristics. For example, low Rossby number flows with the same total energy can have highly variable flow dynamics when they have a major fraction of their energy associated with internal tides, near-inertial waves, or the internal wave continuum [see the results discussed in Thomas and Daniel (2021)]. On the other hand, as Rossby number approaches  $O(1)$  values, even a small amount of unbalanced flow component can make a significant difference in the flow dynamics [see the results discussed in Capet et al. (2008) and Thomas and Vishnu (2022)]. In this idealized study, we focus on tracer dispersion in the latter case, i.e., flows affected by the presence of weak unbalanced flow components. We specifically use the two-vertical-mode model used by Thomas and Vishnu (2022) to study tracer dispersion across different Rossby numbers. Our study is similar to Thomas and Gupta (2022) who examined tracer dispersion by geostrophic flows and wave-dominated flows using a similar two-vertical-mode model in the small Rossby number regime and found that the presence of waves could enhance tracer dispersion in comparison to geostrophic flows. In contrast, here, we examine the role of Rossby number and resulting flow feature changes on tracer dispersion characteristics.

The plan for this paper is as follows: we describe the model and the setup in section 2, present the main results in section 3, and summarize our study in section 4.

## 2. Flow and tracer equations

To investigate passive tracer dispersion across Rossby numbers, we used the two-vertical-mode model studied in Thomas and Vishnu (2022). The model is derived by projecting the primitive equations on the barotropic and a single high baroclinic mode,  $n$ . The model after nondimensionalization takes the form:

$$\begin{aligned} \frac{\partial \zeta_T}{\partial t} + \text{Ro} \nabla \times [\mathbf{v}_T \cdot \nabla \mathbf{v}_T + \mathbf{v}_C \cdot \nabla \mathbf{v}_C + (\nabla \cdot \mathbf{v}_C) \mathbf{v}_C] \\ = f_T - \nu \Delta^8 \zeta_T, \end{aligned} \quad (1a)$$

$$\begin{aligned} \frac{\partial \mathbf{v}_C}{\partial t} + \hat{\mathbf{z}} \times \mathbf{v}_C + \text{Bu} \nabla p_C + \text{Ro}(\mathbf{v}_T \cdot \nabla \mathbf{v}_C + \mathbf{v}_C \cdot \nabla \mathbf{v}_T) \\ = \mathbf{f}_C - \nu \Delta^8 \mathbf{v}_C, \end{aligned} \quad (1b)$$

$$\frac{\partial p_C}{\partial t} + \nabla \cdot \mathbf{v}_C + \text{Ro}(\mathbf{v}_T \cdot \nabla p_C) = -\nu \Delta^8 p_C. \quad (1c)$$

In the above equations, subscripts  $T$  and  $C$  denote the barotropic and baroclinic fields, respectively. Specifically,  $\zeta_T$  and  $\mathbf{v}_T$  represent the barotropic vorticity and velocity, respectively, and  $\mathbf{v}_C$  and  $p_C$  represent the baroclinic velocity and pressure, respectively. Additionally, we obtain two nondimensional parameters in the process of obtaining the nondimensional [(1)]: Rossby number  $\text{Ro} = U/(fL)$  and Burger number  $\text{Bu} = (NH/n\pi fL)^2$ . These two parameters are expressed in terms of the dimensional variables: rotational frequency  $f$ , buoyancy frequency  $N$ , a flow velocity estimate  $U$ , an estimate for the horizontal length scale  $L$ , and an estimate for the vertical length scale  $H$ . Furthermore, the gradient operator in (1) is given as  $\nabla = (\partial/\partial x, \partial/\partial y)$  and the curl operator shorthand used above is  $\nabla \times \mathbf{v} = \nabla \times (u, v) = \partial v / \partial x - \partial u / \partial y$ .

Since the baroclinic mode is a high mode with  $n \gg 1$ , we set  $\text{Bu} = 0.01$ , a small parameter. As explained with the numerical results in Thomas and Arun (2020) using the same model, while the qualitative results regarding the flow would be similar in the  $\text{Bu} \ll 1$  regime, a relatively higher value of  $\text{Bu}$  would slow down the interaction between the two modes while a relatively lower value of  $\text{Bu}$  would speed up the interactions. The forcing terms above,  $f_T$  and  $\mathbf{f}_C$ , are different from conventional forcing schemes that inject a prescribed power into the system. Instead, the forcing terms above were set to maintain a fixed amount of energy at large scales (see specific implementation details of the forcing scheme in the appendix of Thomas and Vishnu 2022). The barotropic forcing  $f_T$  maintained a constant energy level in wavenumbers  $k \leq 5$ , where  $k = |\mathbf{k}| = \sqrt{k_x^2 + k_y^2}$  is the wavenumber vector magnitude corresponding to the horizontal wavenumber vector  $\mathbf{k} = (k_x, k_y)$ . On the other hand, the baroclinic forcing  $\mathbf{f}_C$  maintained the energy level of the spatially homogeneous  $k = 0$  mode, which corresponds to inertial oscillations. The forcings were set such that the barotropic energy was  $O(1)$  and the baroclinic energy level was about 10% of the barotropic energy, and therefore a small perturbation with respect to the barotropic flow. The hyperdissipation terms, i.e., terms with  $\nu \Delta^8$  on the right-hand side of (1), ensured that the flow energy reaching grid scale was dissipated smoothly and provided a clear inviscid inertial range of scales between forced and dissipated scales.

With the above setup, we varied  $\text{Ro}$  from 0.1 to 1, generating different flows in forced-dissipative equilibrium with almost the same energy levels. Waves are contained in the low-energy baroclinic flow, while the high-energy barotropic flow is purely a vortical mode. Although the low-energy baroclinic flow is a small perturbation to the barotropic flow, the baroclinic flow significantly modifies the barotropic flow structures as Rossby number is increased, this being one of the highlights of the results of Thomas and Vishnu (2022). The upshot is that the two-vertical-mode model with a low-energy baroclinic flow generates a barotropic flow with a rich spatiotemporal structure resembling complex submesoscale dynamical features at  $O(1)$  Rossby numbers. These features include a forward-flow energy flux, increased small-scale energy dissipation, and a strong preference for cyclonic coherent vortices over anticyclonic vortices. The barotropic flow generated from the two-vertical-mode model is therefore an idealized

divergence-free two-dimensional flow that shows features of mesoscale and submesoscale flows at low and high Rossby numbers, respectively. In this work, we used this idealized two-dimensional flow to examine tracer dispersion across different Rossby numbers.

Once the flow for a specific  $\text{Ro}$  reached forced-dissipative equilibrium, we started time integrating a passive tracer field  $\theta$  advected by the barotropic flow based on the tracer equation:

$$\frac{\partial \theta}{\partial t} + \mathbf{v}_T \cdot \nabla \theta = f_\theta - \alpha \Delta^8 \theta. \quad (2)$$

The passive tracer field was initialized with random white noise, and then, the tracer forcing,  $f_\theta$  above, forced and maintained the tracer variance at wavenumber  $k = 1$ , i.e., domain scale, using the same technique used for the flow forcing until tracer variance reached a forced-dissipative equilibrium. The hyperdissipation term,  $-\alpha \Delta^8 \theta$  above, dissipated tracer variance at grid scales, thereby allowing the tracer field to attain forced-dissipative equilibrium.

We integrated the flow and tracer equations using the pseudospectral method in a domain  $(x, y) \in [0, 2\pi]^2$  with  $1152^2$  grid points, twice the resolution used by Thomas and Vishnu (2022), giving us the maximum wavenumber as  $1152/2 = 576$  in both  $k_x$  and  $k_y$  directions. We further implemented 2/3 dealiasing in the numerical solver, which set the Fourier coefficients of wavenumbers larger than 2/3 of the maximum wavenumber to 0, to avoid aliasing errors. Consequently, the maximum wavenumber after dealiasing was  $k_{\max} = (2/3) \times 576 = 384$  in each  $k_x$  and  $k_y$  direction. Based on trial numerical integrations, where we monitored the flow structures and energy spectra to ensure that small-scale structures were well resolved and flow energy was dissipated at grid scale, we set hyperdiffusion coefficient for both the flow and tracer fields to  $10^{-34}$ . The statistical quantities discussed in the following section were obtained by time averaging the flow variables after the flow and tracer fields reached equilibrated states. The time averaging window was chosen after successive increments until any further increase had no more effect on the averaged variables. The averaging window varied for different Rossby number flows, with the longest window of several hundred eddy turnover time scales being needed for the low Rossby number flows.

Since we advected the tracer field with the barotropic flow field alone, hereafter we will drop the subscript  $T$  for the barotropic flow, with the understanding that the velocity and vorticity fields correspond to the barotropic flow.

### 3. Tracer dispersion across Rossby numbers

In our numerical integrations, we varied  $\text{Ro}$  in (1) from 0.1 to 1 with increments of 0.1, thus generating 10 flows with different Rossby numbers. The effective Rossby number of each flow was then computed as  $\text{Ro}_{\text{eff}} = \text{Ro} \zeta_{\text{RMS}}$ , where  $\zeta_{\text{RMS}}$  is the root-mean-square value of the barotropic vorticity field. Below, we will discuss the changes in various tracer dispersion features across Rossby numbers. Although we present quantitative statistical details for multiple  $\text{Ro}$ , for convenient

reading, we will present selected plots, especially when showing physical field plots, to limit the number of figures. We will specifically highlight the results for the lowest Rossby number flow with  $\text{Ro}_1 = \text{Ro}_{\text{eff}} = 0.2$  and the highest Rossby number flow with  $\text{Ro}_3 = \text{Ro}_{\text{eff}} = 4.3$ , and occasionally an intermediate flow with Rossby number  $\text{Ro}_2 = \text{Ro}_{\text{eff}} = 1.2$ .

Figure 1 shows the spatial structure of the barotropic vorticity (left column) and the tracer field (right column) with Rossby number increasing from top to bottom. The low Rossby number flow is characterized by an inverse energy flux resulting in the formation of domain-scale, well-defined coherent vortices with roughly equal number of cyclonic and anticyclonic vortices. Increasing Rossby number leads to a forward energy flux for the flow, breaking up of coherent vortices and generating finer-scale structures. Furthermore, the number and size of coherent vortices reduce with increasing Rossby number, along with a preference for cyclonic coherent vortices. These features of the barotropic vorticity, seen in the left column of Fig. 1, are identical to those discussed in great detail in Thomas and Vishnu (2022).

Examining the tracer field features in the right column in Fig. 1, we find that at a low Rossby number, the tracer field is trapped in the cores of coherent vortices: observe in Fig. 1b that blobs of tracer field correspond to the locations of coherent vortices in Fig. 1a. With increasing Rossby number, the generation of small-scale vortical structures accompanying breaking up of coherent vortices enhances tracer stirring. The enhancement in tracer dispersion with increase in Rossby number is clear from examining the right column of Fig. 1 from top to bottom.

The top row of Fig. 2 shows time-averaged horizontal wavenumber spectra for energy and tracer variance for the three flows shown in Fig. 1. Notice that the energy spectra in Fig. 2a overlap for the three flows at low wavenumbers. This is because, as mentioned earlier, all the flows we generated in forced-dissipation equilibrium by forcing wavenumbers  $k \leq 5$  have similar energy levels and the energy of each flow is primarily set by the energy content in large-scale structures or low wavenumbers. With forcing acting at low wavenumbers and dissipation acting at high wavenumbers, we may associate the intermediate wavenumber band  $k \sim 10\text{--}100$  to the inertial range, where the effects of forcing and dissipation are least felt. The inertial range of the spectra in Fig. 2a shows that with increasing Rossby number, the spectra become shallower with more variance at high wavenumbers or small scales; this is expected based on the physical space structures seen in the left column of Fig. 1 showing energetic small-scale structures at high Rossby numbers.

The time-averaged tracer variance horizontal wavenumber spectra in Fig. 2b show striking differences with increasing Rossby number. Since the tracer field was forced and maintained at domain scale with wavenumber  $k = 1$ , all the spectra overlap at  $k = 1$ . However, with increasing Rossby number, we find that the tracer variance content decreases in general across wavenumbers. Specifically, notice that the highest Rossby number tracer spectrum (the red curve) is much below the lowest Rossby number tracer spectrum (the black curve). Tracer variance therefore gets severely depleted

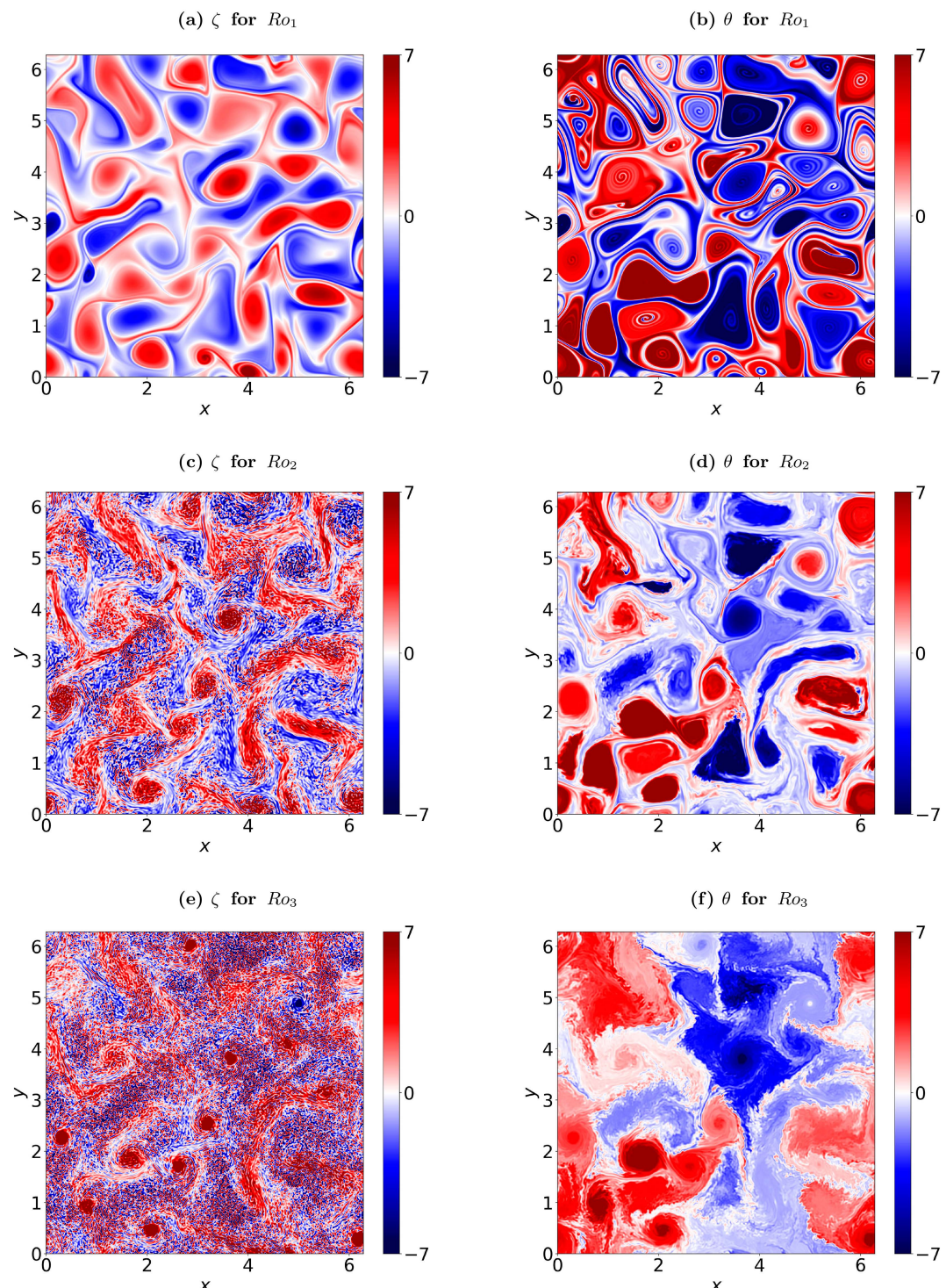


FIG. 1. (left)  $\zeta$  and (right)  $\theta$  for  $Ro_1$ ,  $Ro_2$ , and  $Ro_3$ . Observe the breaking up of large-scale coherent vortices and the generation of small-scale structures on the left column from top to bottom, which corresponds to stronger dispersion of the tracer field in the right column from top to bottom.

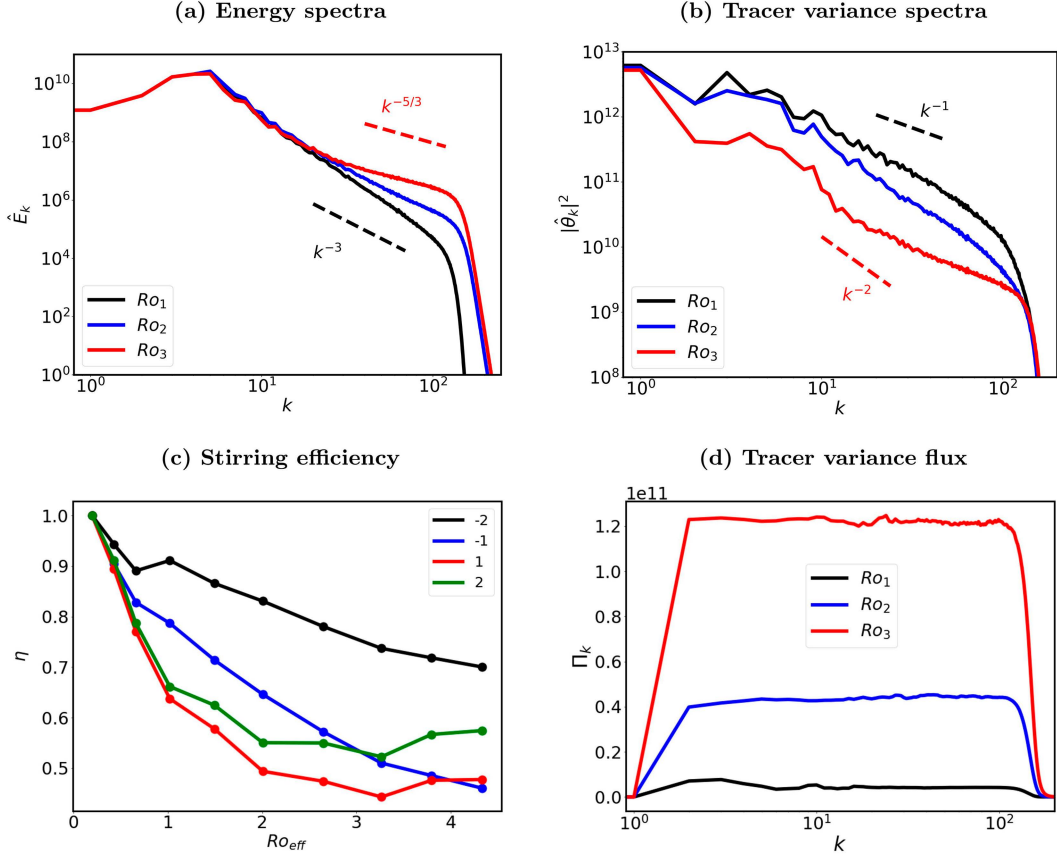


FIG. 2. Time-averaged (a) energy and (b) tracer variance horizontal wavenumber magnitude spectra for three flows with increasing Rossby numbers. Spectral slopes are noted for reference. (c) Stirring efficiency [(4)] for  $q = -2, -1, 1$ , and 2 and (d) time-averaged tracer variance flux

across scales at high Rossby numbers, which is an indication of enhanced stirring. It is also noteworthy in Fig. 2b that the highest Rossby number spectrum is not steeper than the lowest Rossby number spectrum in the wavenumber band  $k \sim 10\text{--}100$ . The depletion of tracer variance across wavenumbers is therefore not accurately captured by the inertial range spectral slope. This signals the limitation of using a single variable, i.e., inertial range slope, to characterize tracer dispersion and stirring.

Given the multiscale nature of the flows we are examining, stirring of the tracer field is variable across spatial scales. To quantify scale-specific stirring, we computed the  $q$ -norm of the tracer field, defined as (Thiffeault 2012)

$$\|\theta\|^{(q)} = \sum_{k \neq 0} (k^{2q} |\hat{\theta}_k|^2)^{1/2}. \quad (3)$$

In the above equation, the tracer variance  $|\hat{\theta}_k|^2$  at a particular scale  $k$  is multiplied by the wavenumber  $k$  raised to a power  $q$  and summed over all the nonzero wavenumbers. Setting  $q > 1$  gives us an estimate for the tracer field at higher wavenumbers or smaller scales, while setting  $q < 1$  gives us the tracer field estimate at small wavenumbers or large scales. The  $q$ -norm therefore provides a weighted estimate of the

tracer field with respect to spatial scales, as detailed in Thiffeault (2012), thereby allowing us to compare the scale-dependent stirring properties of flows. To compare the efficiency of stirring at different scales across Rossby numbers, we calculated the stirring efficiency defined as

$$\eta = \frac{\|\theta\|_{Ro_{\text{eff}}}^{(q)}}{\|\theta\|_{Ro_1}^{(q)}}. \quad (4)$$

We computed  $\eta$  for different Rossby numbers, and the results are shown in Fig. 2c. For all  $q$  values,  $\eta$  is less than 1 for flows with  $Ro_{\text{eff}} > Ro_1$  and further decreases with increasing Rossby number. Since  $\eta$  is defined as the ratio of  $\|\theta\|^{(q)}$  at a specific Rossby number to that at the lowest Rossby number,  $\eta < 1$  indicates that the weighted tracer estimate is relatively lower at the particular Rossby number in comparison to that at the lowest Rossby number. This means that a flow with Rossby number  $Ro_{\text{eff}}$  is more efficient at stirring tracers than the  $Ro_1$  flow, since more efficient stirring leads to faster expulsion of tracer variance to smaller scales, thereby decreasing tracer variance at a particular scale.

It is also interesting to note in Fig. 2c that the  $\eta$  curves drop much more rapidly with increase in  $Ro_{\text{eff}}$  as we go from

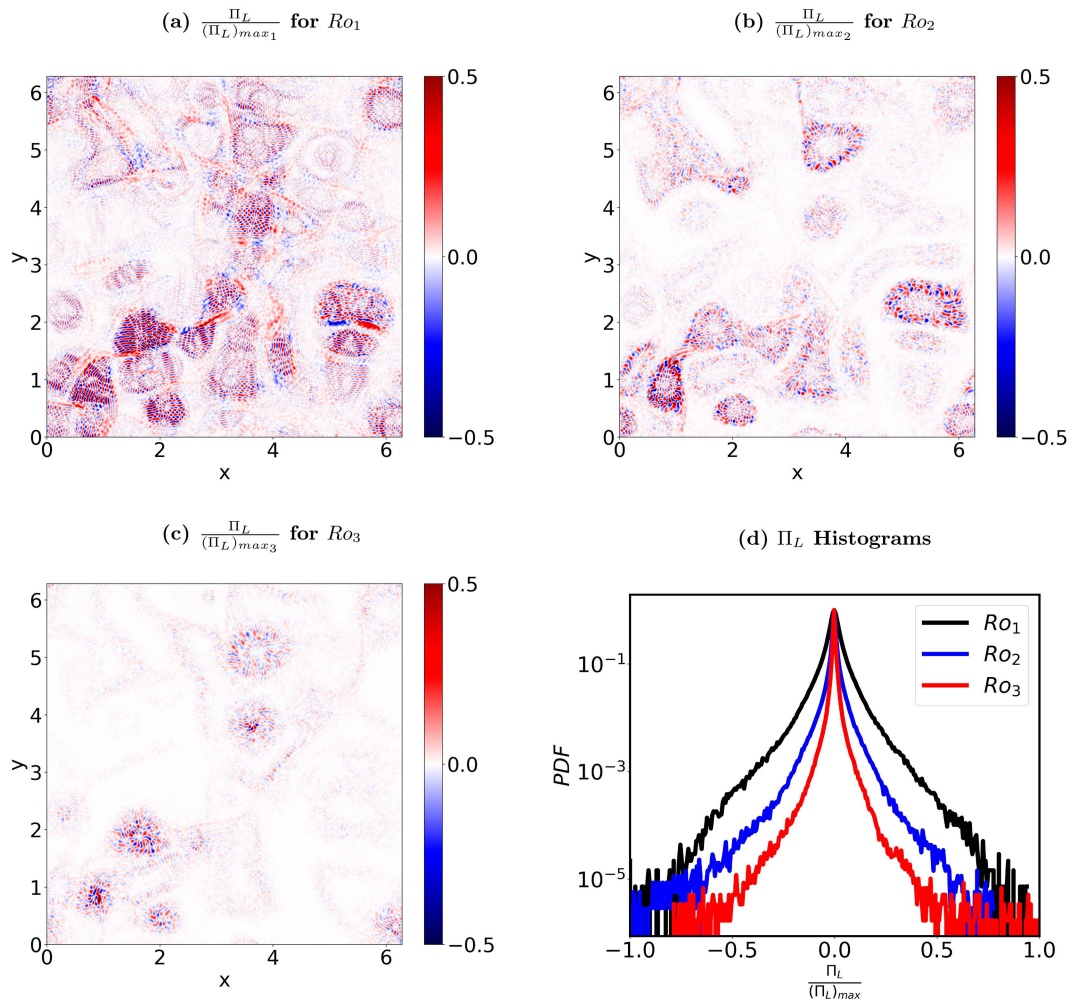


FIG. 3. (a)–(c) Tracer variance flux in physical space normalized by its maximum value for three different Rossby number flows. Notice that the flux is higher in a larger area for  $\text{Ro}_1$  than for  $\text{Ro}_3$ . (d) Histograms of the normalized flux for the three different Rossby number flows. Observe that the histograms are wider for low Rossby numbers than for higher Rossby numbers, indicating that a particular normalized flux value has a higher occurrence at lower Rossby numbers.

negative to positive  $q$  values, indicating that stirring is more efficient at smaller scales than larger scales, as Rossby number increases. Finally, we see that  $q = -1, 1$ , and  $2$  curves are in the same range of  $\eta$  for a high  $\text{Ro}_{\text{eff}}$ , with the three curves intersecting at multiple locations. This is an indication of the fact that for a really high  $\text{Ro}_{\text{eff}}$ , the stirring effects are high at both scales, leading to similar  $\eta$  values for different  $q$  values.

To examine the rate at which tracer variance is stirred downscale, we computed the tracer variance flux. Taking the Fourier transform of (2) and manipulating it gives us

$$\frac{d}{dt} \sum_{p=k_{\max}}^k |\hat{\theta}_p|^2 = \Pi_k + F_k - D_k. \quad (5)$$

In the above equation, the left-hand side represents the rate of change of the tracer variance contained in the band  $[k, k_{\max}]$ , while  $F_k$  and  $D_k$  represent the net forcing and dissipation in the same wavenumber band. The term  $\Pi_k$  represents the

tracer variance flux, indicating the rate at which tracer variance is getting transferred across scales at wavenumber  $k$ . A positive flux implies downscale transfer of tracer variance. Figure 2d shows the time-averaged tracer variance flux for the three different Rossby numbers. The flux increases with Rossby number, with the flux for the largest Rossby number flow,  $\text{Ro}_3$ , being more than an order of magnitude higher than the flux for the smallest Rossby number flow,  $\text{Ro}_1$ . The rate of downscale transfer of tracer variance therefore increases with increasing Rossby number, indicating efficient stirring capabilities of high Rossby number flows.

Examination of tracer variance spectra,  $q$ -norm, and tracer variance flux point toward tracer stirring by flows becoming more efficient with increasing Rossby numbers, which leads to an increased downscale tracer spectral flux and variance depletion at high Rossby numbers. Although the tracer spectral flux reveals increased downscale variance transfer with increasing Rossby number, it does not provide any information

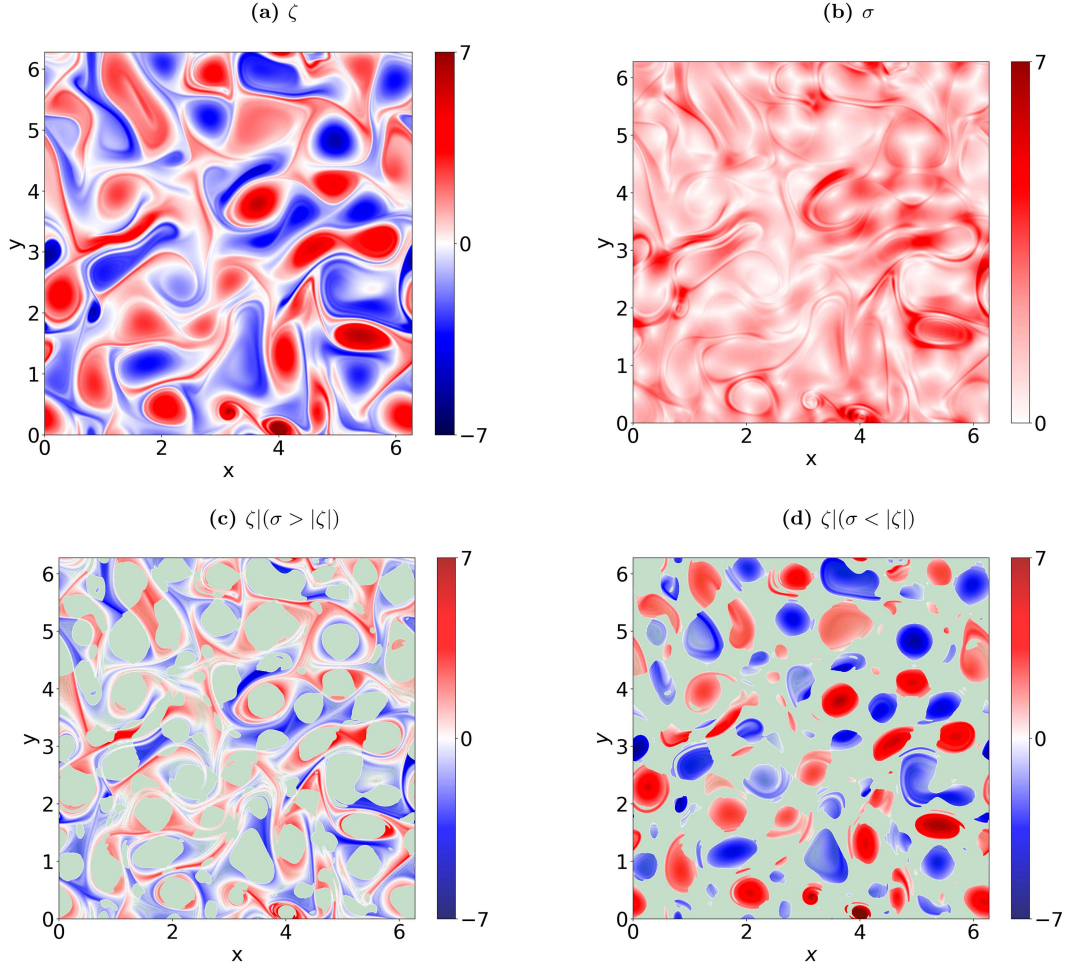


FIG. 4. (a) Barotropic vorticity  $\zeta$ , (b) barotropic strain rate  $\sigma$ , (c)  $\zeta$  restricted to strain-dominant regions, and (d)  $\zeta$  restricted to vorticity-dominant regions, for  $\text{Ro}_1$ . The light green shaded regions in the bottom panels are regions where the field is set to zero. Notice that strain-dominant regions are primarily regions between coherent vortices, while vorticity-dominant regions are almost exclusively well-defined coherent vortices.

regarding the flow structures in physical space and their role in stirring and transferring the tracer variance downscale. We will now investigate the tracer downscale flux in physical space and its connection to flow structures.

We used a filtering operation to construct the flux of tracer variance in physical space, similar to that in Thomas and Gupta (2022), by defining a low-pass filtering operation

$$\tilde{\theta}_L = \mathcal{F}^{-1}[\hat{\theta}(k \leq k_L)], \quad (6)$$

where  $\hat{\theta}$  is the Fourier transform of  $\theta$  and  $\mathcal{F}^{-1}$  denotes the inverse Fourier transform. The  $\tilde{\theta}_L$  is therefore a low-pass filtered tracer field that retains only the large-scale component, i.e., scales larger than  $L$  or wavenumbers smaller than  $k_L = 2\pi/L$ . We apply the low-pass filter to (2) and multiply the resulting equation with  $\tilde{\theta}_L$  and manipulate to get

$$\frac{\partial}{\partial t} \left( \frac{\tilde{\theta}_L^2}{2} \right) + \nabla \cdot [\tilde{\theta}_L \widetilde{\theta v_T}_L] = \underbrace{(\theta v_T)_L \cdot \nabla \tilde{\theta}_L}_{-\Pi_L} + \tilde{F}_L - \tilde{D}_L. \quad (7)$$

The above equation governs the time evolution of tracer variance contained in scales larger than or equal to  $L$ . Integrating over the domain would eliminate the second term on the left-hand side of the above equation, while the first term on the right-hand side would not integrate to zero. The  $\Pi_L$  is the flux of the tracer variance from large to small scales. We examined  $\Pi_L$  and its features for different wavenumbers across the inertial range, and Fig. 3 shows an example flux field for three different Rossby numbers normalized by the maximum flux value with  $k_L = 80$  chosen as the filtering wavenumber.

Figures 3a–c show that the flux takes both positive and negative values, although the net flux is positive and downscale. Furthermore, we find that the flux attains high values more frequently in the lowest Rossby number case in Fig. 3a, while high flux values are less frequent in the highest Rossby number case shown in Fig. 3c. This is quantified in the histogram of the normalized flux shown in Fig. 3d. The normalized flux values have a lower frequency of occurrence at higher Rossby numbers. The standard deviation of the flux histograms

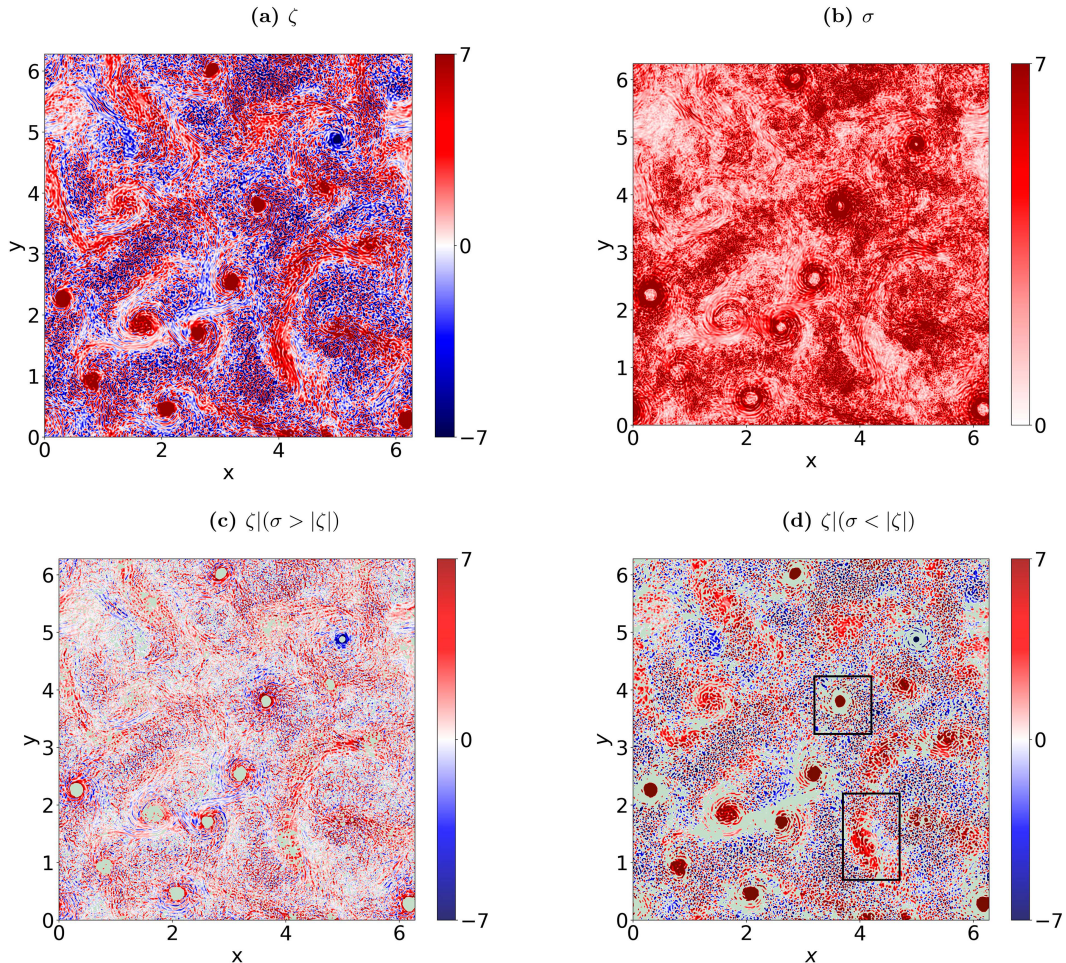


FIG. 5. (a) Barotropic vorticity  $\zeta$ , (b) barotropic strain rate  $\sigma$ , (c)  $\zeta$  restricted to strain-dominant regions, and (d)  $\zeta$  restricted to vorticity-dominant regions, for  $\text{Ro}_3$ . The light green shaded regions in the bottom panels are regions where the field is set to zero. Notice that strain-dominant regions exclude the small coherent vortices, while vorticity-dominant regions consist of small well-defined coherent vortices and small fragmented bits of vorticity. The black rectangular boxes in (d) highlight a coherent vortex and fragmented vorticity pieces.

decreases with increasing Rossby numbers, indicating the inefficiency of tracer stirring at lower Rossby numbers where the flux fluctuates more with respect to the mean compared to higher Rossby numbers. Using different filtering wave-numbers,  $k_L$  gave us similar qualitative results, with the conclusions for  $k_L = 80$  applying for any  $k_L$  across the inertial range. Due to this, hereafter, we will fix  $k_L = 80$  and drop the subscript  $L$  for the physical flux, identifying it as  $\Pi$  for simplicity.

To investigate the distribution of the tracer flux with respect to the flow structures, we divided the flow domain into strain-dominant and vorticity-dominant regions based on the Okubo-Weiss criterion (Okubo 1970; Weiss 1991). Given the barotropic velocity field  $(u, v)$ , the normal strain rate and the shear strain rate were computed as  $\sigma_n = \partial u / \partial x - \partial v / \partial y$  and  $\sigma_s = \partial v / \partial x + \partial u / \partial y$ , respectively. These components were then used to find the total strain rate  $\sigma = \sqrt{\sigma_n^2 + \sigma_s^2}$ . We then partitioned the flow domain as strain-dominant regions,  $\sigma > |\zeta|$ , and vorticity-dominant regions,  $\sigma < |\zeta|$ , where  $\zeta$  is the barotropic vorticity. We maintained strict

inequality to obtain these regions, since only an insignificant number of points satisfied the equality  $\sigma = |\zeta|$ .

[Figure 4a](#) shows the barotropic vorticity field for the lowest Rossby number flow, the same plot shown in [Fig. 1a](#), while [Fig. 4b](#) shows the corresponding strain rate. [Figure 4c](#) shows the barotropic vorticity field constrained to strain-dominant regions. More specifically, this field was obtained by multiplying the vorticity field in [Fig. 4a](#), with 1 at points that satisfied  $\sigma > |\zeta|$  and 0 at points where  $\sigma < |\zeta|$ . Along the same lines, [Fig. 4d](#) shows the barotropic vorticity field constrained to vorticity-dominant regions. Similar results for the highest Rossby number flow are given in [Fig. 5](#).

From the bottom panels of [Fig. 4](#), we find that vorticity-dominant regions are composed almost exclusively of large well-defined coherent vortices, while the sheared regions between coherent vortices belong to strain-dominant regions. In contrast, from the bottom panel of [Fig. 5](#), it is noteworthy that vorticity-dominant regions contain small coherent vortices

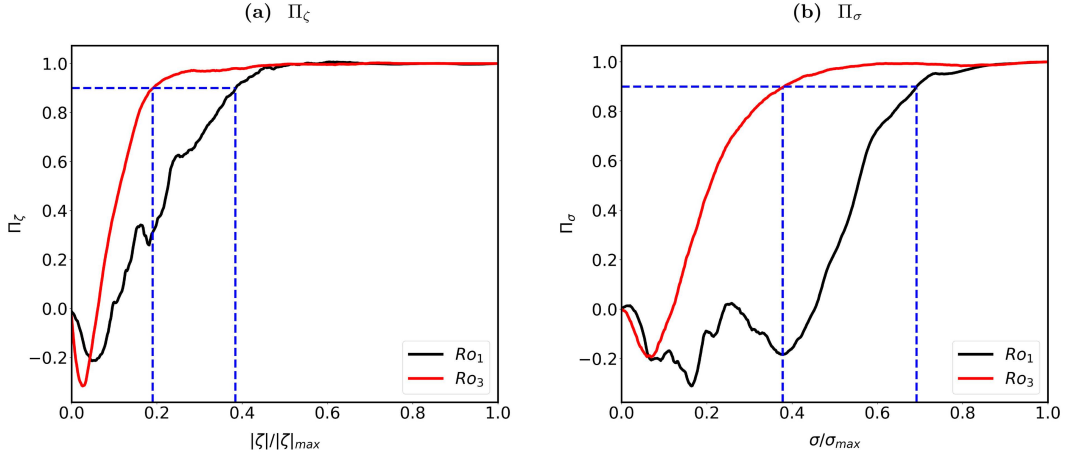


FIG. 6. Distribution of normalized cumulative flux as a function of (a) normalized vorticity magnitude and (b) normalized strain. The dashed horizontal line in each panel denotes 90% cumulative flux, and the dashed vertical lines represent the corresponding normalized vorticity magnitudes and normalized strain rates. The dashed lines in (a) indicate that 90% of flux corresponds to 19% and 38% of the maximum vorticity magnitude for the high and low Rossby number cases, respectively. The dashed lines in (b) indicate that 90% of flux corresponds to 38% and 69% of the maximum strain rate for the high and low Rossby number cases, respectively.

and a lot of small-scale scattered vorticity fragments (high-vorticity regions). The black rectangular boxes in Fig. 5d highlight a small coherent vortex and fragmented vorticity pieces. This feature is a key difference between low and high Rossby number flows that will be relevant for the discussion below: at high Rossby numbers, vorticity-dominant regions contain a lot of incoherent, localized, vorticity fragments, in addition to small coherent vortices.

We further examine how the tracer flux is distributed as functions of vorticity and strain rate. For this, we first used the physical space distribution of tracer flux, vorticity, and strain rate to express the tracer flux  $\Pi$  as a function of the normalized vorticity magnitude  $|\zeta|/|\zeta|_{\max}$  and normalized strain rate  $\sigma/\sigma_{\max}$ , respectively, to obtain  $\Pi(|\zeta|/|\zeta|_{\max})$  and  $\Pi(\sigma/\sigma_{\max})$ . We then used these to find the cumulative flux distribution as a function of normalized vorticity magnitude and normalized strain rate as

$$\Pi_\zeta = \frac{\sum_{s=0}^{s=|\zeta|/|\zeta|_{\max}} \Pi(s)}{\sum_{s=0}^{\infty} \Pi(s)} \quad \text{and} \quad \Pi_\sigma = \frac{\sum_{s=0}^{s=\sigma/\sigma_{\max}} \Pi(s)}{\sum_{s=0}^{\infty} \Pi(s)}. \quad (8)$$

Figure 6 shows  $\Pi_\zeta$  and  $\Pi_\sigma$  for the lowest and highest Rossby number flows. The  $\Pi_\zeta$  is mostly contributed by low vorticity magnitude regions (Fig. 6a): 90% of the flux comes from regions with vorticity less than 19% of the maximum vorticity magnitude for the high Rossby number case and 38% of the maximum vorticity magnitude for the low Rossby number case. We see a similar trend with strain rate in Fig. 6b for the high Rossby number case: 90% of the flux comes from regions with less than 38% of the maximum strain rate. On the other hand, the low Rossby number case in Fig. 6b shows that the flux has major contributions from strain rates below 69% of the maximum strain rate. These reveal that the physical space

regions with high vorticity magnitude and high strain rate are regions where only a small fraction of the net tracer downscale flux is located. This finding is particularly striking at high Rossby numbers, where low vorticity and low strain rate regions are correlated with most of the tracer downscale flux regions.

We further mapped the physical space locations that correspond to 90% of the cumulative tracer flux, and these are shown in Figs. 7 and 8 for the low and high Rossby number cases, respectively. Specifically, the vorticity field in those regions that account for 90% of the net flux, i.e., vorticity regions that lie to the left of the second dashed vertical blue line in Fig. 6a, is highlighted in Fig. 7b. In plotting Fig. 7b, we retained vorticity regions where 90% of the tracer flux is located and zeroed out the remaining regions of the vorticity field, these zeroed out regions being colored light green. On comparing Fig. 7b with the full vorticity field in Fig. 7a, we see that the vortex cores with high vorticity magnitudes at the core are zeroed out or green in Fig. 7b. This indicates that vortex cores are regions that have little contribution toward downscale tracer flux. The physical space regions that correspond to 90% of flux shown in Fig. 7b were then further divided into strain-dominant and vorticity-dominant regions, similar to the procedure used to generate the bottom panels of Fig. 4, and these are shown in Figs. 7c and 7d. These indicate that the strain-dominant regions between coherent vortices and vorticity-dominant regions excluding vorticity cores support the majority of the tracer downscale flux.

Figure 8 shows similar fields for the highest Rossby number case. Notice that the small cyclonic coherent vortices in Fig. 8a are zeroed out or green in Fig. 8b, again indicating that most of the downscale tracer flux is located in regions outside coherent vortices. On further decomposing Fig. 8b into strain-dominant and vorticity-dominant regions, we find that the fragmented pieces of vorticity in the bottom black box in Fig. 5d persists in Fig. 8d, while the coherent vortex in the top black box of Fig. 5d

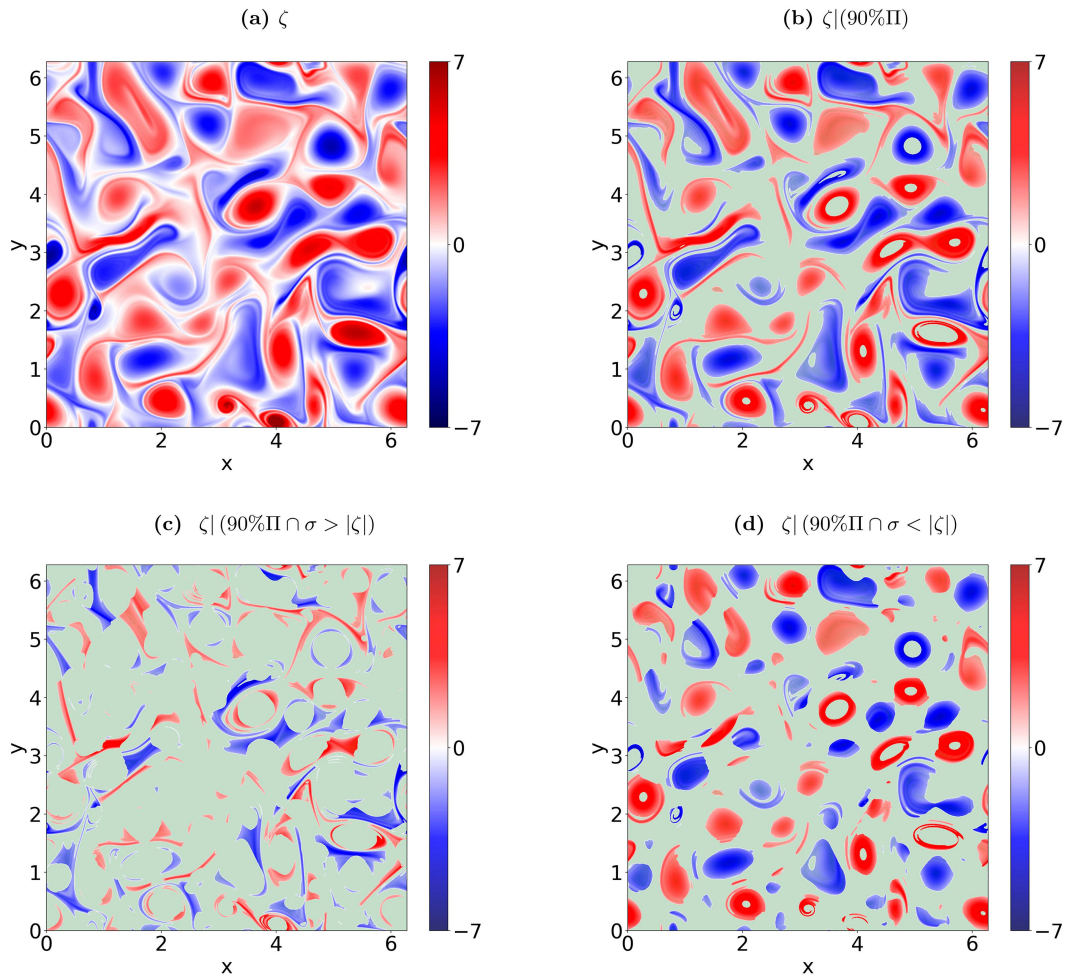


FIG. 7. (a) Full  $\zeta$  field and (b)  $\zeta$  field constrained to regions that contribute 90% of the tracer variance flux, for  $\text{Ro}_1$ . The bottom row shows the field in (b) further constrained to (c) strain-dominant and (d) vorticity-dominant regions. The light green shaded regions in the bottom panels are regions where the field is set to zero.

is zeroed out or green in Fig. 8d. Both the coherent vortex and the fragmented vorticity in the two black boxes in Fig. 5d are vorticity-dominant regions, although only the latter region supports a significant tracer flux. We found this to be a persistent feature after carefully examining several high Rossby number flow fields such as those shown in the bottom panel of Fig. 8 at different well-separated times, namely, vorticity-dominant regions of high Rossby number flows with fragmented vorticity pieces are responsible for most of the downscale tracer flux.

For further clarity on the relative significance of different flow regions for tracer flux, we integrated the tracer flux in strain-dominant and vorticity-dominant regions over the entire domain and computed the fraction of the total flux in these different regions. Figure 9a shows the variation of these fractions as a function of Rossby number. At low Rossby numbers, the flux is mostly associated with strain-dominant regions, outside coherent vortices, as seen in Figs. 4 and 7. On the other hand, at high Rossby numbers, much of the flux is concentrated in vorticity-dominant regions, with regions composed of fragmented vorticity pieces being responsible for

most of the tracer flux at high Rossby numbers (Figs. 5d and 8d). The tracer variance flux therefore goes through a transition across Rossby numbers: most of the flux is located in strain-dominant regions at low Rossby numbers and vorticity-dominant regions at high Rossby numbers.

Interestingly, tracer variance also goes through a transition, although this transition is opposite to that of tracer flux described above. The fraction of tracer variance  $\theta^2$  in strain-dominant and vorticity-dominant regions as a function of Rossby number is shown in Fig. 9b. At low Rossby numbers, we find higher tracer variance in vorticity-dominant regions, which is in line with the first row of Fig. 1: tracer fields are trapped in vortex cores at low Rossby numbers, the vortex cores being vorticity-dominant regions. Recall that these are also regions of low tracer variance flux: at low Rossby numbers, tracer flux is low in vorticity-dominant regions. In contrast, as seen in Fig. 9b, at high Rossby numbers, tracer variance is higher in strain-dominant regions, corresponding to where tracer flux is lower. Therefore, Fig. 9 reveals that the tracer field accumulates more in regions where tracer variance flux is lower, and the

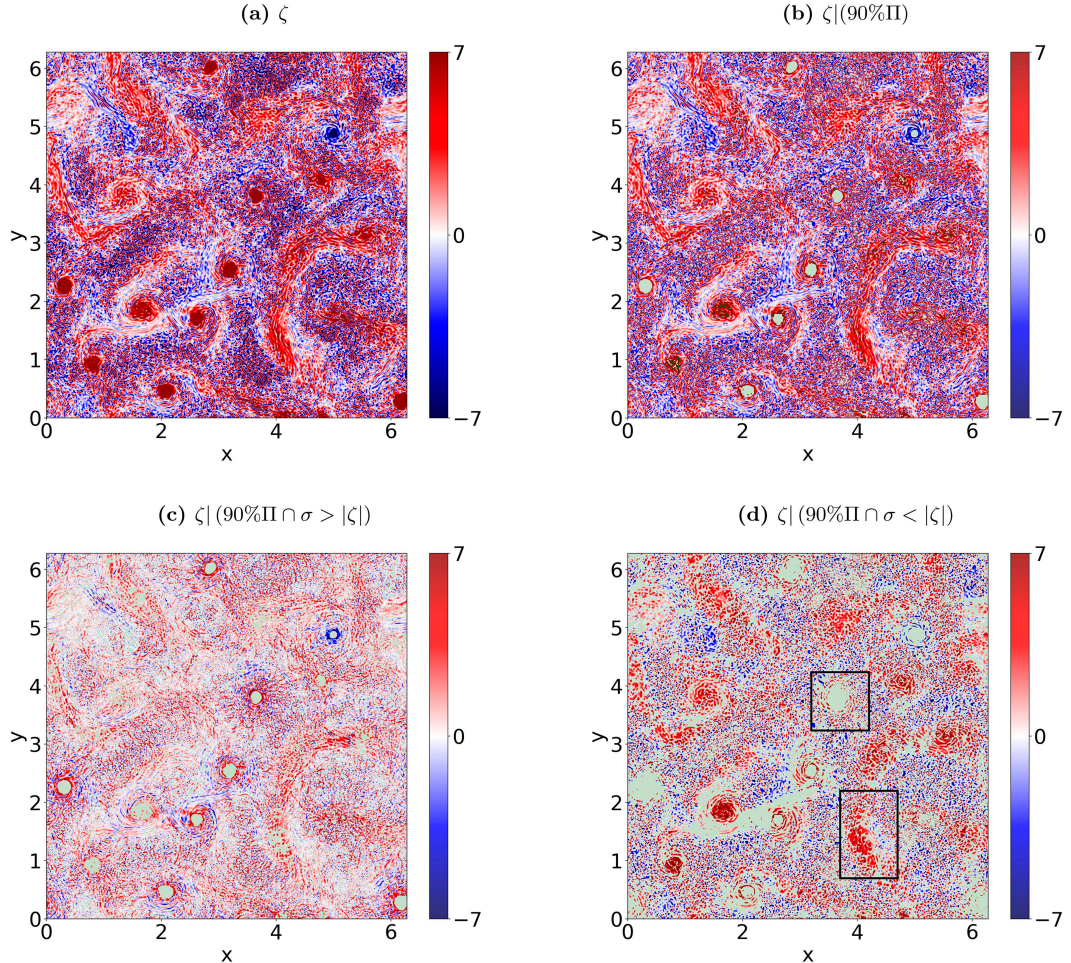


FIG. 8. The vorticity field for the  $\text{Ro}_3$  flow with different constraints. (a) The full  $\zeta$  field and (b) the  $\zeta$  field constrained to regions that contribute 90% of the tracer variance flux. The bottom row shows the field shown in (b) further constrained to (c) strain-dominant and (d) vorticity-dominant regions. The light green shaded regions in the bottom panels are regions where the field is set to zero. In (d), notice that the coherent vortex in the top black box seen in Fig. 5d is zeroed out while the fragmented pieces of vortices in the bottom black box appears, as in Fig. 5d. The physical space region corresponding to fragmented vorticity pieces contribute to the major share of the flux while the coherent vortex does not.

transition across Rossby numbers is opposite for tracer variance flux and tracer variance concentration.

#### 4. Summary and discussion

In this study, we investigated passive tracer dispersion by idealized flows in the low and  $O(1)$  Rossby number regimes. We specifically used the divergence-free two-dimensional barotropic flow from the two-vertical-mode model explored by Thomas and Vishnu (2022). We found that the flow in the low Rossby number regime was composed of well-defined coherent vortices, and these vortices were seen to accumulate blobs of high tracer variance. As Rossby number increased, coherent vortices broke up and generated a lot of small-scale structures, which in turn enhanced the stirring and dispersion of the tracer field. Clear enhancement in tracer dispersion was

observed at higher Rossby numbers compared to low Rossby numbers.

The stirring of the tracer field across different scales was compared using the  $q$ -norm metric, which revealed that stirring was more efficient across all scales, and even more so at smaller scales, as Rossby number increased. Furthermore, the tracer variance spectral flux was an order of magnitude higher for the highest Rossby number flow than for the lowest Rossby number flow, indicating that the downscale transfer of the tracer variance was significantly enhanced at higher Rossby numbers. The tracer variance spectra revealed that the increased stirring led to depletion of the tracer variance across scales at higher Rossby numbers.

We further examined the distribution of the tracer variance flux in physical space, primarily to identify regions where most of the downscale tracer flux was concentrated. This

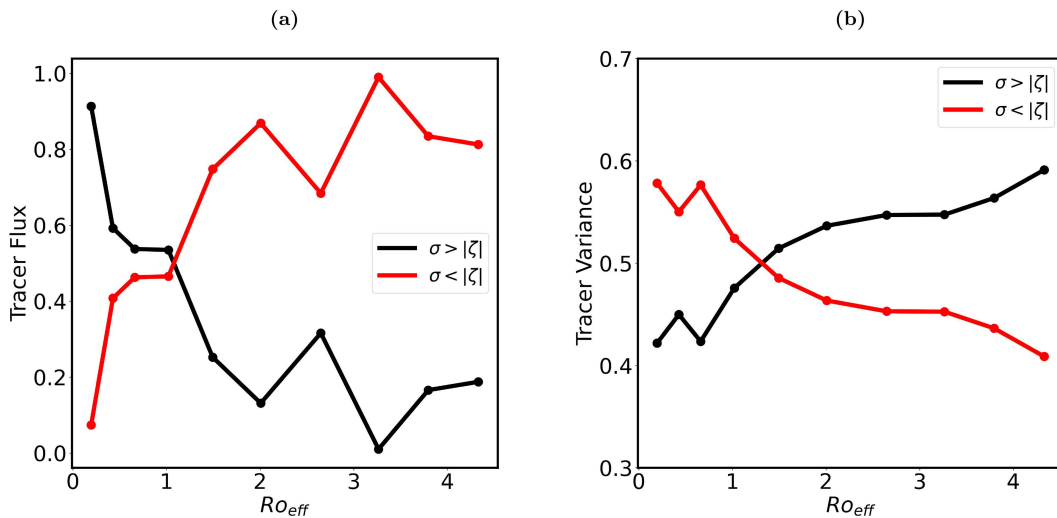


FIG. 9. (a) Fraction of tracer variance flux in strain-dominant and vorticity-dominant regions as a function of Rossby number. (b) Fraction of tracer variance in strain-dominant and vorticity-dominant region as a function of Rossby number.

analysis led to the unexpected conclusion that most of the flux was located in low-vorticity and low-strain regions. Conversely, high-vorticity and high-strain regions, which distinctly stand out in physical space visualizations, were regions that contained much less downscale tracer flux.

Using the Okubo–Weiss criterion to decompose the flow into strain-dominant and vorticity-dominant regions, we found that at low Rossby numbers, the strain-dominated sheared regions between coherent vortices coincided with the largest tracer flux. On the other hand, at high Rossby numbers, vorticity-dominated regions composed of fragmented vortices coincided with the largest tracer variance flux. Furthermore, we found that tracer variance was anticorrelated with the distribution of tracer flux in physical space, i.e., regions that contributed to most of the flux had less tracer variance and vice versa. As a result, tracer variance was high in vorticity-dominated regions for the low Rossby number regime, while tracer variance was high in strain-dominated regions for the high Rossby number regime. This stark change in the physical space regions responsible for the major share of the tracer flux and tracer variance as Rossby number increased from asymptotically small to  $O(1)$  values was an interesting outcome of this study.

Our findings detailed above reveal multiple key features of tracer dispersion by  $O(1)$  Rossby number submesoscale flows that differentiates them from tracer dispersion by small Rossby number mesoscale flows. Of course, the reader will acknowledge that the extreme idealization of the setup we used here, namely, considering only divergence-free two-dimensional flows for advecting the tracer field and ignoring the direct effect of internal waves and other three-dimensional ageostrophic modes, prevents detailed comparisons to be made with realistic flows in the ocean. Nevertheless, some qualitative inferences can still be made. Recall our discussion in the beginning of this paper pointing out enhanced stirring at submesoscales with submesoscale diffusivity often being observed to be an order of magnitude higher than that expected from theoretical

predictions (Shcherbina et al. 2015; Sundermeyer et al. 2020; Kunze et al. 2015; Polzin and Ferrari 2004; Spiro Jaeger et al. 2020; Klymak et al. 2015; Cole and Rudnick 2012; Samelson and Paulson 1988). Some of these diffusivity-measuring experiments injected dye tracers in the ocean and tracked their evolution to measure the width of the dye streaks as a function of time, which was then used to compute tracer diffusivity at those scales. Since we did not introduce tracer locally in our experiments, we do not have a quantitative estimate for tracer diffusivity variation across Rossby numbers. Nevertheless, Fig. 2, revealing an order of magnitude increase in tracer variance flux at  $O(1)$  Rossby numbers compared to small Rossby number, and the tracer field dispersion seen in the right column of Fig. 1 indicate that submesoscale flows can significantly enhance tracer stirring and effective diffusivity, in line with observational results mentioned above.

We conclude this paper by making a comment regarding ocean model parameterizations. As mentioned in the introduction, accurate parameterization of tracer dispersion in ocean models is crucial for predicting several valuable features of the ocean state, including the strength of the large-scale circulation. Large-scale ocean models typically have an isotropic diffusion coefficient along with a Laplacian or higher-order Laplacian term to dissipate tracer fields at small scales. However, as this study shows, the tracer flux and tracer variance organize themselves around different kinds of flow structures, emphasizing the anisotropic nature of tracer dispersion. It may therefore be beneficial to take into account parameters such as the local flow Rossby number and the dynamical properties of the flow when developing subgrid-scale parameterizations in large-scale ocean models.

**Acknowledgments.** J. T. acknowledges financial support from the Science and Engineering Research Board (SERB) of India through the project SRG/2022/001071 and the Deep Ocean Mission scheme of the Ministry of Earth

Sciences (MoES) through the project F.No.MoES/PAMC/DOM/18/2022 (E-12926). M. S. is grateful to the Visiting Students Program at ICTS for funding his stay and covering related expenses during the course of this work.

*Data availability statement.* The datasets used for this work can be accessed at <https://zenodo.org/records/10964493>.

## REFERENCES

- Boccaletti, G., R. Ferrari, and B. Fox-Kemper, 2007: Mixed layer instabilities and restratification. *J. Phys. Oceanogr.*, **37**, 2228–2250, <https://doi.org/10.1175/JPO3101.1>.
- Brannigan, L., D. P. Marshall, A. Naveira-Garabato, and A. J. George Nurser, 2015: The seasonal cycle of submesoscale flows. *Ocean Modell.*, **92**, 69–84, <https://doi.org/10.1016/j.ocemod.2015.05.002>.
- Busecke, J. J. M., and R. P. Abernathey, 2019: Ocean mesoscale mixing linked to climate variability. *Sci. Adv.*, **5**, eaav5014, <https://doi.org/10.1126/sciadv.aav5014>.
- Capet, X., J. C. McWilliams, M. J. Molemaker, and A. F. Shchepetkin, 2008: Mesoscale to submesoscale transition in the California current system. Part I: Flow structure, eddy flux, and observational tests. *J. Phys. Oceanogr.*, **38**, 29–43, <https://doi.org/10.1175/2007JPO3671.1>.
- Chouksey, A., A. Griesel, M. Chouksey, and C. Eden, 2022: Changes in global ocean circulation due to isopycnal diffusion. *J. Phys. Oceanogr.*, **52**, 2219–2235, <https://doi.org/10.1175/JPO-D-21-0205.1>.
- Clément, L., E. Frajka-Williams, K. L. Sheen, J. A. Brearley, and A. C. N. Garabato, 2016: Generation of internal waves by eddies impinging on the western boundary of the North Atlantic. *J. Phys. Oceanogr.*, **46**, 1067–1079, <https://doi.org/10.1175/JPO-D-14-0241.1>.
- Cole, S. T., and D. L. Rudnick, 2012: The spatial distribution and annual cycle of upper ocean thermohaline structure. *J. Geophys. Res.*, **117**, C02027, <https://doi.org/10.1029/2011JC007033>.
- Ferrari, R., and C. Wunsch, 2009: Ocean circulation kinetic energy: Reservoirs, sources and sinks. *Annu. Rev. Fluid Mech.*, **41**, 253–282, <https://doi.org/10.1146/annurev.fluid.40.111406.102139>.
- Gnanadesikan, A., M.-A. Pradal, and R. Abernathey, 2015: Isopycnal mixing by mesoscale eddies significantly impacts oceanic anthropogenic Carbon uptake. *Geophys. Res. Lett.*, **42**, 4249–4255, <https://doi.org/10.1002/2015GL064100>.
- Gula, J., M. J. Molemaker, and J. C. McWilliams, 2015: Topographic vorticity generation, submesoscale instability, and vortex street formation in the Gulf Stream. *Geophys. Res. Lett.*, **42**, 4054–4062, <https://doi.org/10.1002/2015GL063731>.
- Holloway, G., and S. S. Kristmannsson, 1984: Stirring and transport of tracer fields by geostrophic turbulence. *J. Fluid Mech.*, **141**, 27–50, <https://doi.org/10.1017/S0022112084000720>.
- Klein, P., A. M. Treguier, and B. L. Hua, 1998: Three-dimensional stirring of thermohaline fronts. *J. Mar. Res.*, **56**, 589–612, <https://doi.org/10.1357/002224098765213595>.
- Klymak, J. M., W. Crawford, M. H. Alford, J. A. MacKinnon, and R. Pinkel, 2015: Along-isopycnal variability of spice in the North Pacific. *J. Geophys. Res. Oceans*, **120**, 2287–2307, <https://doi.org/10.1002/2013JC009421>.
- Kunze, E., J. M. Klymak, R. C. Lien, R. Ferrari, C. M. Lee, M. A. Sundermeyer, and L. Goodman, 2015: Submesoscale water-mass spectra in the Sargasso Sea. *J. Phys. Oceanogr.*, **45**, 1325–1338, <https://doi.org/10.1175/JPO-D-14-0108.1>.
- Lien, R.-C., and T. B. Sanford, 2019: Small-scale potential vorticity in the upper-ocean thermocline. *J. Phys. Oceanogr.*, **49**, 1845–1872, <https://doi.org/10.1175/JPO-D-18-0052.1>.
- McWilliams, J. C., 2016: Submesoscale currents in the ocean. *Proc. Roy. Soc.*, **A472**, 20160177, <https://doi.org/10.1098/rspa.2016.0117>.
- Okubo, A., 1970: Horizontal dispersion of floatable particles in the vicinity of velocity singularities such as convergences. *Deep-Sea Res. Oceanogr. Abstr.*, **17**, 445–454, [https://doi.org/10.1016/0011-7471\(70\)90059-8](https://doi.org/10.1016/0011-7471(70)90059-8).
- Poje, A. C., T. M. Özgökmen, D. J. Bogucki, and A. D. Kirwan Jr., 2017: Evidence of a forward energy cascade and Kolmogorov self-similarity in submesoscale ocean surface drifter observations. *Phys. Fluids*, **29**, 020701, <https://doi.org/10.1063/1.4974331>.
- Polzin, K. L., and R. Ferrari, 2004: Isopycnal dispersion in NATRE. *J. Phys. Oceanogr.*, **34**, 247–257, [https://doi.org/10.1175/1520-0485\(2004\)034<0247:IDIN>2.0.CO;2](https://doi.org/10.1175/1520-0485(2004)034<0247:IDIN>2.0.CO;2).
- Ragen, S., M. A. Pradal, and A. Gnanadesikan, 2020: The impact of parameterized lateral mixing on the Antarctic circumpolar current in a coupled climate model. *J. Phys. Oceanogr.*, **50**, 965–982, <https://doi.org/10.1175/JPO-D-19-0249.1>.
- Samelson, R. M., and C. A. Paulson, 1988: Towed thermistor chain observations of fronts in the subtropical North Pacific. *J. Geophys. Res.*, **93**, 2237–2246, <https://doi.org/10.1029/JC093iC03p02237>.
- Scott, R. K., 2006: Local and nonlocal advection of a passive scalar. *Phys. Fluids*, **18**, 116601, <https://doi.org/10.1063/1.2375020>.
- Shcherbina, A. Y., E. A. D'Asaro, C. Lee, J. M. Klymak, M. J. Molemaker, and J. C. McWilliams, 2013: Statistics of vertical vorticity, divergence, and strain in a developed submesoscale turbulence field. *Geophys. Res. Lett.*, **40**, 4706–4711, <https://doi.org/10.1002/grl.50919>.
- , and Coauthors, 2015: The LatMix summer campaign: Submesoscale stirring in the upper ocean. *Bull. Amer. Meteor. Soc.*, **96**, 1257–1279, <https://doi.org/10.1175/BAMS-D-14-00015.1>.
- Siegelman, L., P. Klein, P. Rivière, A. F. Thompson, H. S. Torres, M. Flexas, and D. Menemenlis, 2020: Enhanced upward heat transport at deep submesoscale ocean fronts. *Nat. Geosci.*, **13**, 50–55, <https://doi.org/10.1038/s41561-019-0489-1>.
- Smith, K. S., and R. Ferrari, 2009: The production and dissipation of compensated thermohaline variance by mesoscale stirring. *J. Phys. Oceanogr.*, **39**, 2477–2501, <https://doi.org/10.1175/2009JPO4103.1>.
- Spiro Jaeger, G., J. A. MacKinnon, A. J. Lucas, E. Shroyer, J. Nash, A. Tandon, J. T. Farrar, and A. Mahadevan, 2020: How spice is stirred in the Bay of Bengal. *J. Phys. Oceanogr.*, **50**, 2669–2688, <https://doi.org/10.1175/JPO-D-19-0077.1>.
- Sundermeyer, M. A., D. A. Birch, J. R. Ledwell, M. D. Levine, S. D. Pierce, and B. T. K. Cervantes, 2020: Dispersion in the open ocean seasonal pycnocline at scales of 1–10 km and 1–6 days. *J. Phys. Oceanogr.*, **50**, 415–437, <https://doi.org/10.1175/JPO-D-19-0019.1>.
- Thiffeault, J.-L., 2012: Using multiscale norms to quantify mixing and transport. *Nonlinearity*, **25**, R1, <https://doi.org/10.1088/0951-7715/25/2/R1>.
- Thomas, J., 2023: Turbulent wave-balance exchanges in the ocean. *Proc. Roy. Soc.*, **479A**, 20220565.
- , and S. Arun, 2020: Near-inertial waves and geostrophic turbulence. *Phys. Rev. Fluids*, **5**, 014801, <https://doi.org/10.1103/PhysRevFluids.5.014801>.
- , and D. Daniel, 2021: Forward flux and enhanced dissipation of geostrophic balanced energy. *J. Fluid Mech.*, **911**, A60, <https://doi.org/10.1017/jfm.2020.1026>.

- , and A. Gupta, 2022: Wave-enhanced tracer dispersion. *J. Geophys. Res. Oceans*, **127**, e2020JC017005, <https://doi.org/10.1029/2020JC017005>.
- , and R. Vishnu, 2022: Turbulent transition of a flow from small to  $O(1)$  Rossby numbers. *J. Phys. Oceanogr.*, **52**, 2609–2625, <https://doi.org/10.1175/JPO-D-21-0270.1>.
- Thompson, A. F., A. Lazar, C. Buckingham, A. C. Naveira Garabato, G. M. Damerell, and K. J. Heywood, 2016: Open-ocean submesoscale motions: A full seasonal cycle of mixed layer instabilities from gliders. *J. Phys. Oceanogr.*, **46**, 1285–1307, <https://doi.org/10.1175/JPO-D-15-0170.1>.
- Vladoiu, A., R. C. Lien, and E. Kunze, 2022: Two-dimensional wavenumber spectra on the horizontal submesoscale and vertical finescale. *J. Phys. Oceanogr.*, **52**, 2009–2028, <https://doi.org/10.1175/JPO-D-21-0111.1>.
- Weiss, J., 1991: The dynamics of enstrophy transfer in two-dimensional hydrodynamics. *Physica D*, **48**, 273–294, [https://doi.org/10.1016/0167-2789\(91\)90088-Q](https://doi.org/10.1016/0167-2789(91)90088-Q).
- Yu, X., A. C. Naveira Garabato, A. P. Martin, C. E. Buckingham, L. Brannigan, and Z. Su, 2019: An annual cycle of submesoscale vertical flow and restratification in the upper ocean. *J. Phys. Oceanogr.*, **49**, 1439–1461, <https://doi.org/10.1175/JPO-D-18-0253.1>.